

# Broadband Compact Single-Pole Double-Throw Silicon Photonic MEMS Switch

Alain Yuji Takabayashi<sup>1</sup>, Graduate Student Member, IEEE, Hamed Sattari<sup>2</sup>, Pierre Edinger<sup>3</sup>, Peter Verheyen<sup>4</sup>, Kristinn B. Gylfason, Member, IEEE, Wim Bogaerts<sup>5</sup>, Fellow, IEEE, and Niels Quack<sup>6</sup>, Senior Member, IEEE

**Abstract**—Photonic Integrated Circuits (PICs) benefit from the technology advances in the semiconductor industry to incorporate an ever-increasing number of photonic components on a single chip to create large-scale photonic integrated circuits. We here present a broadband, compact and low-loss Silicon Photonic MEMS switch based on a Single-Pole Double-Throw (SPDT) architecture, where curved electrostatic actuators mechanically displace a movable input waveguide to redirect the optical signal on chip efficiently to either of two output waveguides. The photonic switch has been fabricated in an established silicon photonics technology platform with custom MEMS release post-processing. With a compact footprint of  $65 \times 62 \mu\text{m}^2$ , the switch exhibits an extinction ratio exceeding 23 dB over 70 nm optical bandwidth, a low insertion loss and a fast response time below 1  $\mu\text{s}$ , meeting the requirements for integration in large-scale reconfigurable Photonic Integrated Circuits. [2020-0391]

**Index Terms**—Microelectromechanical systems, photonic integrated circuits, silicon photonics, photonics, optical switch.

## I. INTRODUCTION

THE field of Electronic Integrated Circuits (ICs) has experienced a remarkable development throughout the past decades, which has led to circuits with billions of switching transistors on a single chip, underpinning much of modern day computing. Equivalently, the field of Photonic Integrated Circuits (PICs) has recently seen tremendous progress in integration, whereby tens of thousands of optical components can be operated on a single chip. Among the enabling components

Manuscript received December 22, 2020; revised January 29, 2021; accepted February 14, 2021. Date of publication February 26, 2021; date of current version March 16, 2021. This work was supported by the European Union's Horizon 2020 Research and Innovation Programme under Grant 780283 (MORPHIC - www.h2020morphiceu). The work of Hamed Sattari was supported by the Hasler Foundation under Grant 17008. The work of Niels Quack was supported by the Swiss National Science Foundation (SNSF) under Grant 183717. Subject Editor C. Lee. (Corresponding author: Alain Yuji Takabayashi.)

Alain Yuji Takabayashi, Hamed Sattari, and Niels Quack are with the École Polytechnique Fédérale de Lausanne (EPFL), 1015 Lausanne, Switzerland (e-mail: alain.takabayashi@epfl.ch; hamed.sattari@epfl.ch; niels.quack@epfl.ch).

Pierre Edinger and Kristinn B. Gylfason are with the Division of Micro and Nanosystems, School of Electrical Engineering and Computer Science, KTH Royal Institute of Technology, 100 Stockholm, Sweden (e-mail: edinger@kth.se; gylfason@kth.se).

Peter Verheyen is with the Interuniversity Microelectronics Centre (imec), 3001 Leuven, Belgium (e-mail: peter.verheyen@imec.be).

Wim Bogaerts is with the Department of Information Technology, Ghent University, 9052 Ghent, Belgium, also with the Interuniversity Microelectronics Centre (imec), 9052 Ghent, Belgium, and also with the Center for Nano- and Biophotonics, Ghent University, 9052 Ghent, Belgium (e-mail: wim.bogaerts@ugent.be).

Color versions of one or more figures in this article are available at <https://doi.org/10.1109/JMEMS.2021.3060182>.

Digital Object Identifier 10.1109/JMEMS.2021.3060182

in PICs are optical switches, which allow for efficient routing of light on-chip.

Optical switching in PICs is commonly implemented using the thermo-optic, electro-optic, or plasma dispersion effect. Recently, optical switching by exploiting mechanical effects in PICs has gained interest [1], primarily due to the potential for compact, low-loss and low-power optical switches. Several types of photonic MEMS switches have been demonstrated in the past years, with in-plane and out-of-plane moving electrostatic devices being the most prevalent [2]–[5].

The functionality of an integrated circuit, whether it be electronic or photonic, is determined as much by the performance of constituent elements as by the extent of their connectivity. By scaling up the number of devices in a single circuit, the richness of its connectivity is enhanced, thereby enabling increased complexity, such as dense, on-chip switching networks [4]. In the pursuit of large-scale integration, several criteria must be observed: photonic components should present low optical loss, have a small footprint, consume little power, and ideally, be compatible with existing technology platforms [6].

While designs of similar devices have been introduced conceptually for GaAs platforms previously [7], we here present a new type of photonic switch with single-pole double-throw (SPDT) topology that uses a compact electrostatic MEMS actuator. The device is implemented in a standard silicon photonics technology platform with a few custom post-processing steps, and achieves broadband transmission, high extinction ratio (ER), and low insertion loss (IL), making it suitable for large-scale integration.

## II. OPERATING PRINCIPLE AND DESIGN

The Silicon Photonic MEMS switch is based on a single side suspended movable input waveguide, which can be displaced by curved electrostatic actuators to redirect the optical signal to either one of two output waveguides, as shown in the schematic top view diagram in Figure 1. The input consists of a freestanding, single mode silicon photonic strip waveguide, with a height of 220 nm, width of 450 nm and a length of 23.4  $\mu\text{m}$ . The waveguide is freestanding and anchored on one side, which serves as a mechanical clamp and optical connection to the photonic circuit. The central part of the waveguide incorporates a 70 nm thick shuttle with 220 nm high wings that serve as movable electrodes for the electrostatic actuators. The design values and dimensions are summarized in Table I.

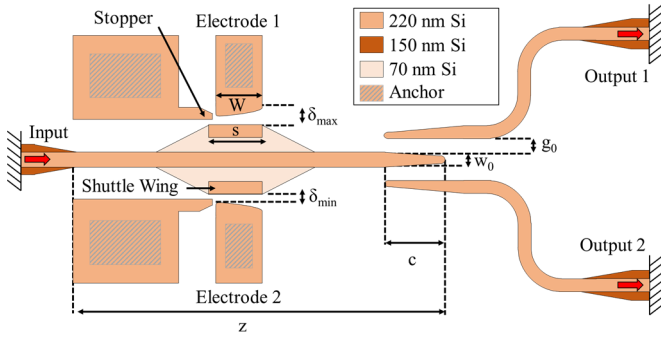


Fig. 1. Schematic diagram of the photonic MEMS switch showing the single side suspended input, which is free to move at its free end towards either of the two suspended, fixed outputs under the influence of an electrostatic force produced at the anchored, curved electrostatic actuators.

TABLE I  
SILICON PHOTONIC MEMS SWITCH DESIGN PARAMETERS

Symbol	Quantity	Value
$g_0$	Initial coupling gap	400 nm
$w_0$	Waveguide width	450 nm
$c$	Coupling length	2.7 $\mu\text{m}$
$W$	Electrode width	5 $\mu\text{m}$
$\delta_{max}$	Maximum electrode-shuttle distance	700 nm
$\delta_{min}$	Minimum electrode-shuttle distance	200 nm
$s$	Shuttle wing length	5.8 $\mu\text{m}$
$z$	Length of input waveguide	23.4 $\mu\text{m}$

The design of the initial coupling gap  $g_0$ , waveguide width  $w_0$ , and coupling length  $c$  are defined by the optical functionality, while the remaining dimensions are defined by the electromechanical behavior. As highlighted schematically by hatched areas in the figure, the stopper and electrodes are also anchored to the substrate, as the undercut resulting from a timed etch step used to release the waveguides only partially removes the oxide under these regions.

The device, including all optical, mechanical, and electrical components has a footprint of  $65 \times 62 \mu\text{m}^2$ . Including the MEMS cavity used for electrical contact and isolation and optical transitions to the oxide-clad parts of the circuit, the unit cell of this device is approximately  $120 \times 150 \mu\text{m}^2$ , which is comparable to the dimensions of switches used in previously demonstrated large-scale switch matrices [4].

### A. Operating Principle

Conceptually, the device is the optical analog of the electrical single-pole double-throw switch [8]: the input signal can be switched to either output upon mechanical movement. In the IDLE state, the input waveguide is perfectly centered between the two output waveguides with a gap separation equal to  $g_0$ , resulting in only residual light coupling in equal amounts to both output branches (Figure 2a). Note, that the device is rarely operated in this mode: light is almost always coupled exclusively to either of the two outputs, where there is a high extinction ratio.

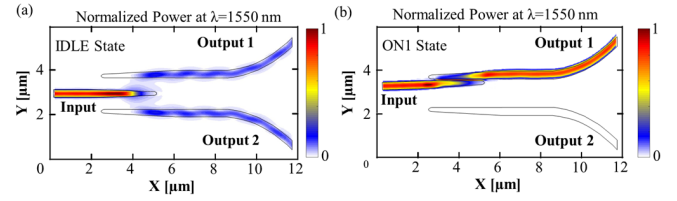


Fig. 2. Distribution of optical power (normalized to the maximum intensity) between the input and output waveguides (a) IDLE state where only a small amount of residual light is coupled to the outputs (b) ON1 state for which light is completely coupled to output 1.

By applying an actuation voltage to electrode 1 (while keeping the input waveguide grounded), an electric field builds up between the electrode and the raised regions of the shuttle's wings. The resulting attractive electrostatic force pulls the movable shuttle and attached input waveguide towards fixed electrode 1, thereby decreasing the coupling gap between the input waveguide and the waveguide of output 1. This smaller coupling gap  $g < g_0$  couples the optical power carried in the input waveguide preferentially to output 1, and as the gap is further decreased by increasing the applied voltage, it is eventually completely coupled to output 1 (Figure 2b), resulting in the ON1 state. Applying potential to the other electrode produces the ON2 state.

The mechanical stoppers indicated in Figure 1 are designed to limit the maximum displacement of the input waveguide to when it comes in contact with the output waveguide, i.e.,  $g \cong 0 \text{ nm}$ . In this manner, the input waveguide should not further push against the output waveguide, which could cause it to bend or deform. Additionally, in order to prevent an electrical short upon contact between the movable shuttle and the stoppers, the two regions are biased at the same voltage as the input waveguide. This zero-gap separation is one of the ON states for the active output. While this design prevents contact between the waveguide and electrode, further improvements towards limiting displacement can be achieved by for example adding a second pair of mechanical stoppers to the right side of the electrodes.

### B. Optical Design

The switch is designed for single-mode operation for photonic signals in the telecom C-Band, i.e. 1530 nm – 1565 nm. We use a 220 nm thick and 450 nm wide silicon strip waveguide, which provides low-loss, single-mode operation within the C-band. The use of strip waveguides is motivated by the desire for small bending radii in the output waveguides, enabling a compact device. On the moveable shuttle, however, rib waveguides are used, to maximize the actuation electrode surface (and thus the electrostatic force) in the raised regions on the wings, while still isolating optically the light-carrying region in the center. The tapers on the input and output of the shuttle are used to provide an adiabatic transition between the strip and rib waveguide structures and minimize optical losses associated with an abrupt step transition. Furthermore, the input and output waveguides are tapered from 450 nm down to 200 nm over the coupling region. This approach allows for short coupling lengths, and has

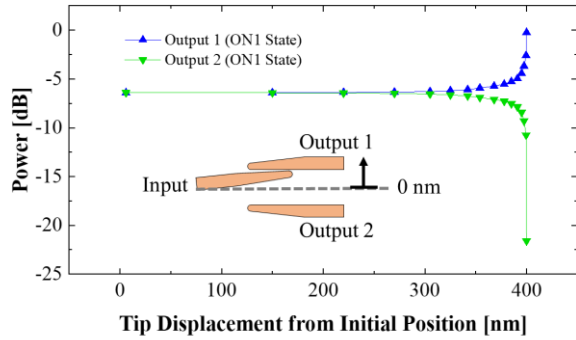


Fig. 3. Simulated power transmission versus gap between input and output waveguides for the ON1 state. An even distribution of power to output 1 and output 2 can be observed for zero tip displacement and a complete transmission of power to output 1 occurs at a tip displacement of 400 nm. The input waveguide is tilted with respect to the output ( $\approx 1^\circ$ ), so there is variation in the gap along the coupling length; however, because this bending angle is small and the suspended waveguide is long, it can be treated as uniform.

the added benefit of increasing the optical bandwidth of the device.

The optical coupling mechanism is evanescent field coupling, i.e. the closer the waveguides, the better the coupling. The relationship between coupling gap and coupling length has been analyzed in various analytical models for standard directional couplers [9]. However, the complex geometry is difficult to describe by simple analytical models, and we hence revert to numerical simulation of the coupled waveguide modes based on a commercial 3D finite difference time domain (FDTD) solver (Lumerical), which provides a convenient and fast approach to extracting the relationship of optical power versus coupling gap.

Optical design of the device using a 3D-FDTD model begins with simulating an ideal ON state with maximum coupling and minimal losses. Optical power coupling between the waveguide tips can be achieved simply with two long ( $> 5 \mu\text{m}$ ), 450 nm rectangular slab waveguides separated by a small coupling gap (i.e.,  $g_0 = 0 \text{ nm}$ ). However, the abrupt ending of the tip is lossy and such a generic structure is long. By introducing adiabatic tapering on the input waveguide, and keeping the output waveguide straight, there is a smooth transition in geometry-related effective index change and losses are reduced. In order to achieve symmetric behavior, and to reduce the effect of an abrupt index transition, the other side of the input waveguide and the outer side of the output tips are also tapered. Here, as the input waveguide decreases in width (from 450 nm to the minimum of 200 nm dictated by the lithography), the outputs get wider and we have strong coupling. The coupling length is also adjusted because when it is too long we have beating, and when it is too short, we have a lossy, abrupt transition. Finally, the coupling gap is increased to ensure an IDLE state with  $< -5 \text{ dB}$  transmission to either output.

The sequential approach outlined above leads to the optimized optical design parameters as listed in Table I. Figure 3 illustrates the power transmission for the optimized design from the input waveguide to the outputs as a function of the

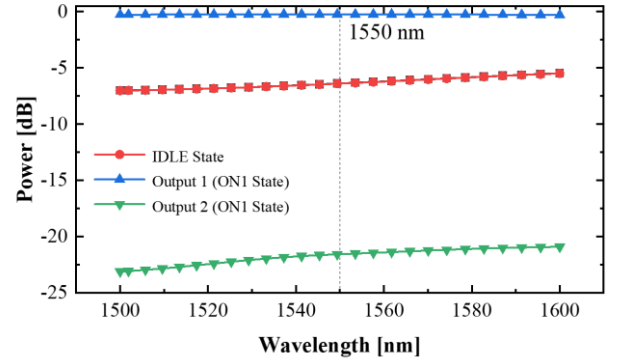


Fig. 4. Simulated wavelength sweep of the power to each of the outputs for the IDLE state as well as the ON1 state for which all input power is transferred to output 1; the low wavelength-dependence of the optical transfer characteristic indicates broadband behavior.

gap between the input and output waveguides. As the gap between the input waveguide and that of output 1 decreases, we see enhanced coupling and therefore a higher power transmission into output 1. At the same time, the complementary gap between the input waveguide and that of output 2 increases and we see a corresponding decrease in power transmission to output 2.

Optical simulation of the photonic MEMS switch over a range of wavelengths in the IDLE state and the ON1 state in which input power is transferred entirely to output 1 (Figure 4) confirms the broadband behavior resulting from the adiabatic coupler design. The optical characteristics for the ON2 state, where the input power is now transferred entirely to output 2 is not illustrated, but is symmetric to that shown. In this case, the power transmission to output 2 is at a maximum and that of output 1 is at a minimum.

### C. Electromechanical Design

The design of the electrostatic actuator and the mechanical suspension is imposed by the requirement to achieve 400 nm displacement for full optical power transfer. We limit the actuation voltage to a maximum of 40 V for compatibility with standard driving electronics. In order to establish the boundaries of the design space, a simplified analytical model of an ideal electrostatic actuator is used, described by the initial gap distance  $d_0$ , the suspension spring constant  $k$ , and the actuator electrode surface  $A$ . The operation of the actuator is in pull-in mode wherein the electrostatic attraction between the raised wings and electrodes exceeds the restoring mechanical spring force. This force imbalance pulls the movable input waveguide towards one output waveguide, increasing optical coupling. Ignoring fringing fields and assuming a small gap spacing, which allows for a 1-dimensional electric field distribution, it is possible to derive an expression for the pull-in voltage.

$$V_{\text{pull-in}} = \sqrt{\frac{8kd_0^3}{27A}} \quad (1)$$

For this simplified model, pull-in occurs at one third the initial gap,  $d_0$ , which is directly related to the optical design.

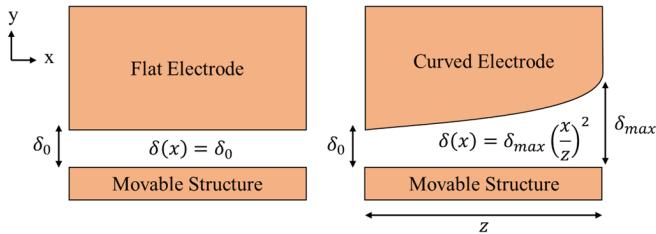


Fig. 5. Flat versus curved electrode, where the latter exhibits a gradual increase in the gap spacing from left to right, towards the tip.

Specifically, the initial coupling gap of 400 nm required for 0 to 100% power transmission represents this initial gap ( $d_0 = g_0$ ). We use this pull-in voltage as the parameter to be optimized, subject to the constraints of fabrication limits and the desire for small form factor. For a transversely loaded beam with rectangular cross-sectional area and spring stiffness corresponding to clamped-free boundary conditions  $k$ , we find that (1) predicts a pull-in voltage ranging from 5 V for a  $12 \mu\text{m}$  beam to 20 V for a  $6 \mu\text{m}$  long beam with the same cross sectional area. As expected, increasing the length of the movable structure decreases the required pull in voltage.

The parallel plate model underestimates the pull-in voltage because by construction it decouples the spring stiffness from the geometric dependence of the system's capacitance. Our use of the transversely loaded cantilever's stiffness and cross-sectional area simply provided an approximation of the expected pull-in voltage for minimal dimensions. In order to refine the analysis, the electromechanical behavior can be described by a cantilever-electrode arrangement, where geometry defines both the electrical and mechanical behavior. For example, the distributed electrostatic force can be represented as a bending moment applied to the cantilever tip instead of a transverse point load at the tip, or, the deflection of the beam can be derived using the derivative of the system capacitance function [10]. Both models predict pull-in to occur at a larger gap of approximately 46% of the initial gap  $d_0$ , rather than the standard 33%. For the same minimal dimensions and cantilever lengths of  $12 \mu\text{m}$  and  $6 \mu\text{m}$  as before, the pull-in voltages increase to 10 V and 35 V, respectively.

A variation on this second approach using a curved electrode, as shown below in Figure 5, provides an advantage over the flat electrode in that larger displacements are achievable with the same initial gap.

In particular, in the case of a flat electrode, the electrostatic force is constant along the length of the movable structure and at one third the initial spacing,  $\delta_0$ , pull-in occurs. For the curved electrode, though, the force is initially strongest at one end (left pictured) but as the movable portion is pulled towards the electrode, the force becomes noticeable over a greater length of the electrode [11]. Pull-in occurs first at the left end, at one third of  $\delta_0$ , but at the right end, where the tip of the structure lies, pull-in doesn't occur until one third of  $\delta_{max} > \delta_0$ . Thus, it is possible to obtain larger displacements with a curved electrode geometry because  $\delta_0$  does not need to be set to the desired displacement and can be made smaller. In this manner, the curved electrode provides a better trade-off when it comes to pull-in characteristics versus form factor.

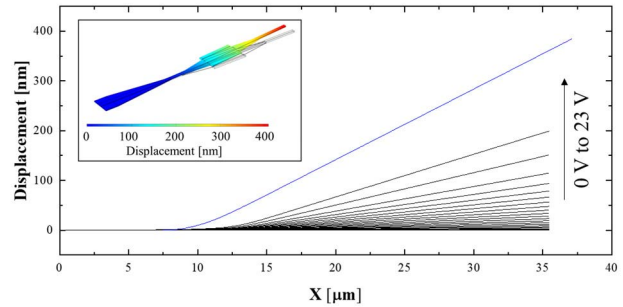


Fig. 6. Simulated deflection along the length of the movable input waveguide as a function of the applied voltage at the active electrode. Pull-in occurs at 23 V and as indicated, achieves the 400 nm waveguide tip deflection.

Additionally, as shown by Legtenberg, by increasing the order of the polynomial defining the electrode curvature, ( $n = 2$  for this design), the beam bending can be constrained, which leads to a stable system (i.e., no pull-in) exhibiting characteristic “zipping” behavior [11]. This additional design parameter allows the same device with different electrode geometry to be used as a digital switch, with abrupt transitions, like in this design, as well as an analog coupler that uses a more gradual transition to smoothly modulate optical transmission.

The designed structure is not an idealized cantilever of rectangular cross-section with distributed load acting along the entire length. Rather, as indicated in Figure 1, the actual movable portion of the structure consists of a rib waveguide with raised wings, serving as the counter-electrodes, two tapers into and out of the rib waveguide, and an extension to the end of the moveable input waveguide. This structure produces a composite cross-section consisting of several discrete and unique cross-sections. Furthermore, the position-dependent force is not applied along the entire length of the moveable portion, but rather only along the shuttle wings, leading to the form of the Euler-Bernoulli equation

$$\frac{d^4 w}{dx^4} = \frac{q(x)}{EI(x)}, \quad (2)$$

where  $w(x)$  is the beam deflection,  $q(x)$  is a distributed load,  $E$  is the Young's modulus, and  $I(x)$  is the area moment of inertia. This form takes into account the area moment of inertia's dependence on position along the movable input, i.e., the cross section of the input varies in both width and height from fixed to free end. A closed-form solution to this differential equation for our exact geometry becomes computationally untenable in symbolic form. Instead, a systematic approach involving the division of the complex structure into small slices, to each of which (2) can be applied, and then recombined, is required. As this is the approach employed by the finite element method (FEM), we employ a commercial FEM software (COMSOL) to model our geometry and simulate for a range of applied voltages until the solutions fail to converge. This condition indicates pull-in has occurred and it can be verified whether the desired 400 nm of displacement have been achieved (Figure 6).

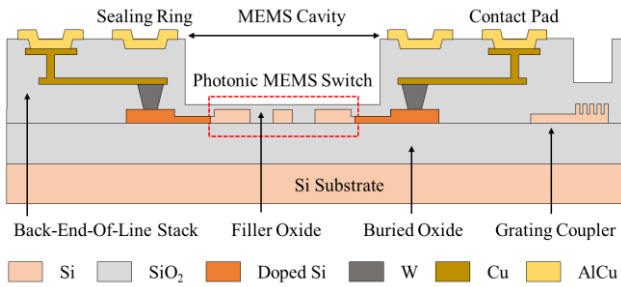


Fig. 7. Cross-section of the iSiPP50G platform with the photonic MEMS switch fabricated in the silicon device layer above the buried oxide of a silicon-on-insulator (SOI) wafer; electrical contact is made via the contact pads, which connect to the doped device layer via the metallization layers in the BEOL stack.

Despite the apparent complex geometry, simulation results indicate that the device in fact operates much like a standard rigid shuttle attached to a hinge. For low to moderate voltages, the displacement increases gradually. Then, as expected, at the pull-in voltage, the tip of the input waveguide snaps to the full displacement allowed by the stoppers and maximum optical transmission is achieved.

An additional optimization parameter is given by the mechanical response time of the electromechanical design. In particular, while a switch that could reconfigure a connection within the approximately 20 ns lifetime of a 400-Gb/s link data packet ( $> 50$  MHz switching speed) would be ideal [12], such performance has not yet been demonstrated in MEMS. However, with appropriate design, the mechanical resonance frequency can be increased by stiffening the suspension (e.g. a shorter cantilever), at the expense of a higher actuation voltage. For the design in Table I, FEM simulations predict that the mechanical resonance frequency in the corresponding eigenmode occurs at approximately 1.18 MHz, which corresponds to a mechanical switching time of 847 ns.

### III. FABRICATION

The Silicon Photonic MEMS switch is fabricated in IMEC's iSiPP50G standard silicon photonics platform. This approach allows for the integration of user-designed devices alongside library-standard, passive and active devices, such as low-loss waveguides, and high-speed modulators, respectively [13]. A representative cross-section of the platform is shown in Figure 7.

The photonic MEMS switch is fabricated within the silicon device layer (DL) of a silicon-on-insulator (SOI) wafer, which in silicon photonics applications serves as the optical core. The DL lies atop a buried oxide (BOX), which typically serves as a cladding material to confine optical signals, but here, is used as the sacrificial layer in the release process. The MEMS cavity is defined by a back-end-of-line (BEOL) etch removing the oxide and other layers above the silicon DL. Additional components include the metallization and contact pads for providing electrical contact to the doped silicon DL, the grating coupler for optical input/output, and an optional sealing ring, which has not been used in this demonstration.

As MEMS are currently non-standard components in this platform, additional post-processing to release the devices

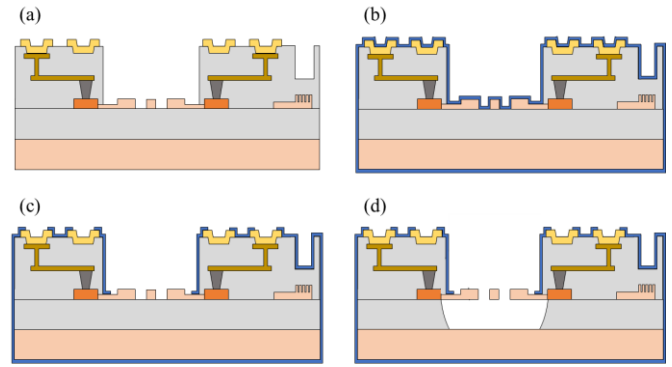


Fig. 8. (a) Selective removal of filler oxide by BHF, (b) Conformal alumina deposition by ALD, (c) Patterning of alumina over the MEMS cavity and contact pads, (d) Removal of sacrificial oxide by vapor-phase HF (VHF).

must be performed following fabrication at IMEC. The release process, schematically depicted in Figure 8 was developed and performed at the Center of MicroNanoTechnology (CMi) at EPFL. Samples are diced into coupons with a  $2 \times 2$  chip configuration and although processing is performed on coupon- and chip-scale, it is fully compatible on wafer-scale. Processing begins with the selective removal of the filler oxide above the DL with a timed buffered HF (BHF) etch (Figure 8a). This step allows the 50 nm of alumina deposited in the subsequent atomic layer deposition (ALD) step to conformally cover the DL, thereby protecting the BEOL stack in the concave corners of the MEMS cavity (Figure 8b). A patterning step employing maskless lithography allows the photoresist patterning over alumina to be done on coupon-scale and allowed for quick adjustment of the mask design. Following the lithography, a controlled dry and wet etch removes the alumina from within the MEMS cavity and over the contact pads and sealing rings (Figure 8c). Dry etching presents a risk for overetching the DL and wet etching negatively affects the metallization, so the two etching steps are performed separately. At this point, an optional dicing step can be performed to divide the coupon into four individual chips. The final step is the removal of the buried oxide below the photonic MEMS switches by vapor-phase HF (VHF), which facilitates a stiction-free release of suspended components.

The optical microscope image and SEM micrograph in Figure 9 show the photonic MEMS switch and surroundings post-release and identify the salient features and components.

### IV. CHARACTERIZATION AND DISCUSSION

The photonic MEMS switches are characterized using the setup schematically outlined in Figure 10.

The optical signal is coupled from a tunable laser (Agilent 81682A, tuning 1510 nm – 1580nm) to the photonic MEMS switch via one of the fibers in the  $10 \times 1$  fiber array (FA) and into the input grating coupler indicated in Figure 9. The light propagates through the device and the amount coupled to each of the outputs is read by a corresponding power sensor (Agilent 81536A) connected to the output grating couplers

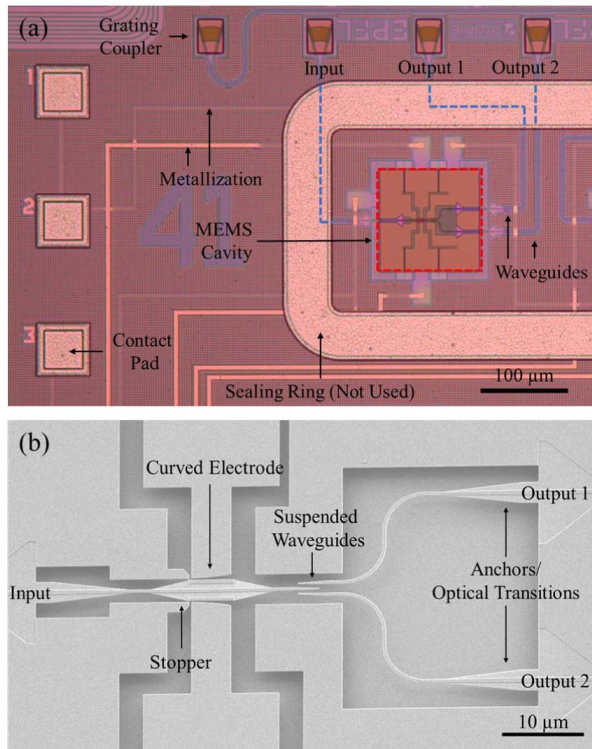


Fig. 9. (a) Optical microscope image showing the MEMS cavity where the photonic MEMS switch is located. Electrical connectivity (contact pad and metallization) and optical input/output via grating couplers and waveguides are also shown (b) SEM micrograph of released device showing suspended waveguides as well as the curved electrodes and mechanical stoppers.

through the FA. The actuation voltage is applied by a custom multi-contact DC probe, whose probe tip pitch matches that of the contact pads on chip. This probe can be connected to a standard DC power supply (0 to 40 V range) for DC measurements or to a waveform generator (with optional voltage amplifier with fast slew rate, not shown in Figure 10) for transient measurements to characterize switching time. In the latter case, an oscilloscope is connected to the analog outputs of the photodetectors, which allows the modulation of the optical signal by the photonic MEMS switch to be observed in the electrical domain.

Functionality of our photonic MEMS switch is demonstrated by tuning the input wavelength to 1550 nm and observing the power at each output as the gap between input and output waveguides decreases/increases with the applied DC actuation voltage. As indicated in Figure 11, for an applied voltage of 22 V on electrode 1, input power is almost completely transferred to output 1 for an ER of approximately 25 dB at 1550 nm. Applying this same voltage to electrode 2 reveals a symmetric characteristic, with output 2 this time receiving all the power.

It is worth noting that with no voltage applied to either electrode (IDLE state), the observed power distribution is not completely symmetric as designed. Instead, we have a 3 dB difference and the crossing indicating 0 dB of difference is shifted to the right by approximately 12 V. This discrepancy can be attributed to a combination of two phenomena: asymmetric relaxation of the mechanical boundary conditions at

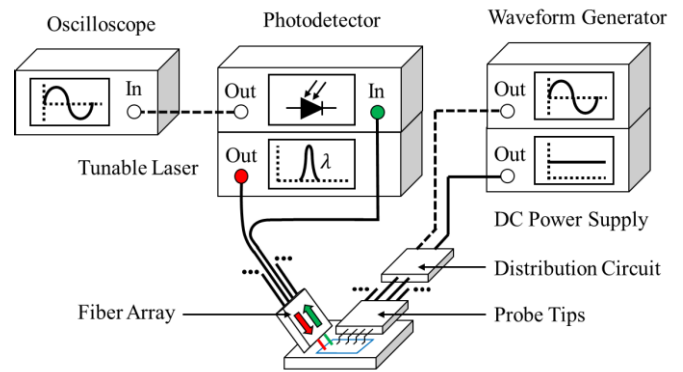


Fig. 10. Light from the tunable laser is coupled into/out of the device via a fiber array and the transmitted power is recorded at the photodetector. For steady-state measurements, the actuation voltage is applied by the probe tips connected to the DC power supply. For transient measurements, the waveform generator provides the actuation voltage and the output is read from the oscilloscope, which is connected to the analog output of the photodetector.

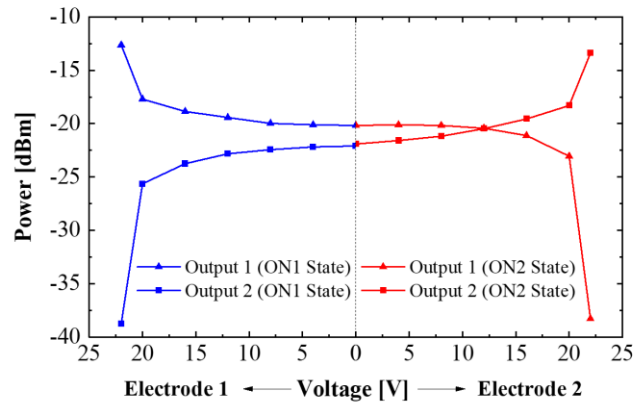


Fig. 11. Optical power to each output as a function of applied voltage for  $\lambda = 1550 \text{ nm}$ ; the red curves indicate power to output 1 and output 2 when the bottom electrode (electrode 2) is active and the blue curves indicate power distribution between outputs when the top electrode (electrode 1) is active. Measurement performed for an input laser power of 0 dBm.

the anchored and free edges of the input waveguide during the VHF release can lead to the input bending preferentially toward one output. Additionally, there may be loss variation in the optical path between the two outputs related to the optical transitions and grating couplers. Nevertheless, this shift in the balanced zero state can be compensated for by applying a systematic offset voltage.

Performing this same type of DC measurement for a range of wavelengths allows us to characterize the spectral response of our photonic MEMS switch. The result (Figure 12) of a sweep across the entire C-band for both ON states, i.e., all power to output 1 and all power to output 2, reveals significant broadband behavior.

In particular, we observe that our device maintains an average ER larger than 23 dB over the entire 70 nm, achieving a maximum at 1550 nm, as designed. The ER exhibits a slightly stronger dispersive behavior than predicted by FDTD simulation (Figure 4) which can be attributed to variations in the grating couplers due to fabrication and misalignment and

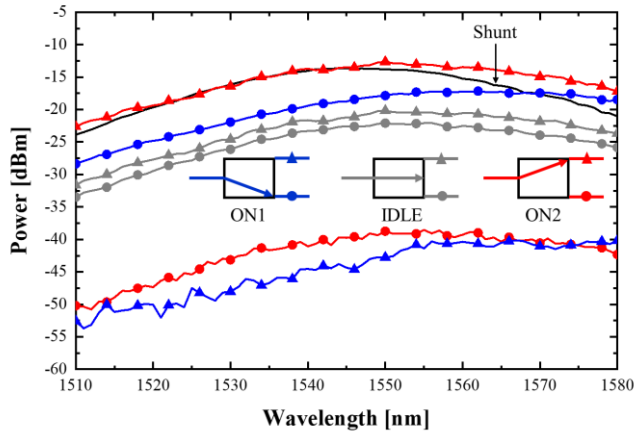


Fig. 12. Power distribution between outputs as a function of wavelength; average ER > 23 dB maintained over full 70 nm wavelength sweep; ER of 25 dB at  $\lambda = 1550$  nm. Measurement performed for an input laser power of 0 dBm.

results in specific peak transmission and dispersion characteristics for each grating coupler. Thus, upon characterization of the device using two fiber grating couplers (i.e., one for input and one for output), the observed spectral response is a superposition of the two grating coupler spectral responses on top of the device's nominally flat characteristic.

Comparison of the measurement results with simulations reported in Figure 3, reveals a difference of approximately 12 dB in maximum power transmission. This offset comes from the fact that losses in the passive devices, i.e., grating couplers, transitions, and waveguides are included in the reported measurements. We choose here to report the measured data rather than normalized results. In particular, as part of the alignment procedure of the fiber array to the device, we use a shunt connection between two grating couplers to determine the chip position with optimal power transmission. A different set of grating couplers is then used to inject and sense light that passes through the switch. Ideally, by normalizing measurements to those of this initial shunt connection, it is possible to extract the IL of the switch. However, any offset of the fiber core with respect to its ideal position over the center of the grating coupler leads to variation in coupling efficiency, peak wavelength, and symmetry in power transmission. The alignment fiber-grating coupler pair already introduces a misalignment error and each subsequent pair up to those used for input and output adds additional error. Thus, without a chain of identical devices, where the contribution of each additional device can be precisely isolated, it is only possible to provide a confidence range for the IL, which in this case is < 0.4 dB between 1520 and 1545 nm.

The third experiment evaluates the dynamic behavior of our photonic MEMS switch. We applied a rectangular pulse as the actuation voltage and measured the switching behavior by converting the optical signal via an amplified high-speed photodiode and feeding the electrical output to an oscilloscope. Figure 13 shows the switching times from IDLE to ON1 and from ON1 to IDLE for our device, which as depicted, are 822 ns and 736 ns, respectively. The fast switching time can be

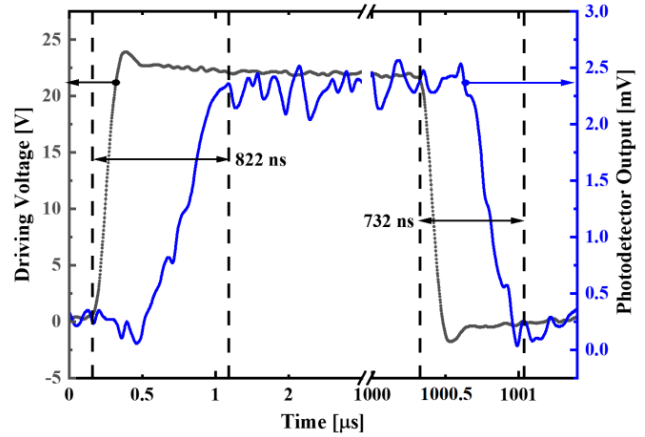


Fig. 13. A 23 V amplitude driving voltage is applied to one of the electrodes to trigger pull-in of one output (ON1 state). 822 ns after the driving signal goes high, our SPDT switch responds and the optical output is recorded as an electrical signal on an oscilloscope. Correspondingly, when the driving signal goes low, the switch responds 732 ns afterwards.

attributed to both the steep, non-linear behavior of the device around pull-in and the use of low-resistance, doped silicon for electrical contacting. Stiffer geometries could be used to further reduce switching time, but doing so would come at the cost of a higher pull-in voltage.

In addition to the 0 to 100% switching demonstrated here, this device can also be used to perform other functions, such as variable attenuation. By changing the curvature of the electrode, the pull-in characteristics can be made less abrupt, allowing the coupling behavior to be tuned more continuously.

## V. CONCLUSION

We have presented the design, simulation, fabrication, and characterization of a new photonic MEMS switch in an established silicon photonics platform. The SPDT topology and curved electrodes offer a unique approach to effectively couple light (> 23 dB ER) over a wide range of wavelengths. By using an adiabatic tapered design, the switch offers broadband behavior, with a bandwidth greater than 70 nm in the C-band. The curved electrodes and stiff geometry, allow the steep non-linear pull-in characteristics to provide quick switching below 1  $\mu$ s with an applied voltage of 23 V. With these performance parameters, this SPDT silicon photonic MEMS switch presents itself as an attractive component to be used in dense switch matrices and more generally, as a versatile analog or digital coupler, or variable attenuator, in multipurpose PICs.

## ACKNOWLEDGMENT

Alain Takabayashi thanks Dr. Marcell Kiss for his assistance in setting up the transient measurement.

## REFERENCES

- [1] C. Errando-Herranz, A. Y. Takabayashi, P. Edinger, H. Sattari, K. B. Gylfason, and N. Quack, "MEMS for photonic integrated circuits," *IEEE J. Sel. Topics Quantum Electron.*, vol. 26, no. 2, Mar. 2020, Art. no. 8200916, doi: [10.1109/ISTQE.2019.2943384](https://doi.org/10.1109/ISTQE.2019.2943384).
- [2] S. Han, T. J. Seok, N. Quack, B.-W. Yoo, and M. C. Wu, "Large-scale silicon photonic switches with movable directional couplers," *Optica*, vol. 2, no. 4, pp. 370–375, Apr. 2015, doi: [10.1364/OPTICA.2.000370](https://doi.org/10.1364/OPTICA.2.000370).

- [3] T. Nagai and K. Hane, "Silicon photonic microelectromechanical switch using lateral adiabatic waveguide couplers," *Opt. Exp.*, vol. 26, no. 26, pp. 33906–33917, Dec. 2018, doi: [10.1364/OE.26.033906](https://doi.org/10.1364/OE.26.033906).
- [4] T. J. Seok, N. Quack, S. Han, R. S. Muller, and M. C. Wu, "Highly scalable digital silicon photonic MEMS switches," *J. Lightw. Technol.*, vol. 34, no. 2, pp. 365–371, Jan. 15, 2016, doi: [10.1109/JLT.2015.2496321](https://doi.org/10.1109/JLT.2015.2496321).
- [5] Q. Qiao, M. S. Yazici, B. Dong, X. Liu, C. Lee, and G. Zhou, "Multifunctional mid-infrared photonic switch using a MEMS-based tunable waveguide coupler," *Opt. Lett.*, vol. 45, no. 19, pp. 5620–5623, Oct. 2020, doi: [10.1364/OL.400132](https://doi.org/10.1364/OL.400132).
- [6] N. Quack *et al.*, "MEMS-enabled silicon photonic integrated devices and circuits," *IEEE J. Quantum Electron.*, vol. 56, no. 1, Feb. 2020, Art. no. 8400210, doi: [10.1109/JQE.2019.2946841](https://doi.org/10.1109/JQE.2019.2946841).
- [7] M. L. Povinelli *et al.*, "Design of a nanoelectromechanical high-index-contrast guided-wave optical switch for single-mode operation at 1.55  $\mu\text{m}$ ," *IEEE Photon. Technol. Lett.*, vol. 15, no. 9, pp. 1207–1209, Sep. 2003, doi: [10.1109/LPT.2003.816706](https://doi.org/10.1109/LPT.2003.816706).
- [8] J. Oberhammer, M. Tang, A.-Q. Liu, and G. Stemme, "Mechanically tri-stable, true single-pole-double-throw (SPDT) switches," *J. Micromech. Microeng.*, vol. 16, no. 11, pp. 2251–2258, Sep. 2006, doi: [10.1088/0960-1317/16/11/001](https://doi.org/10.1088/0960-1317/16/11/001).
- [9] L. Chrostowski and M. Hochberg. (Mar. 2015). Silicon photonics design: From devices to systems. Cambridge Core. Accessed: Mar. 31, 2020. [Online]. Available: <https://core/books/silicon-photonics-design/BF3CF13E8542BCE67FD2BBC7104ECEAB>
- [10] G. O'Brien, D. J. Monk, and L. Lin, "MEMS cantilever beam electrostatic pull-in model," *Proc. SPIE*, vol. 4593, pp. 31–41, Nov. 2001, doi: [10.1117/12.448834](https://doi.org/10.1117/12.448834).
- [11] R. Legtenberg, J. Gilbert, S. D. Senturia, and M. Elwenspoek, "Electrostatic curved electrode actuators," *J. Microelectromech. Syst.*, vol. 6, no. 3, pp. 257–265, 1997, doi: [10.1109/84.623115](https://doi.org/10.1109/84.623115).
- [12] B. G. Lee *et al.*, "Silicon photonic switch fabrics in computer communications systems," *J. Lightw. Technol.*, vol. 33, no. 4, pp. 768–777, Feb. 15, 2015, doi: [10.1109/JLT.2014.2371616](https://doi.org/10.1109/JLT.2014.2371616).
- [13] M. Pantouvaki *et al.*, "Active components for 50 Gb/s NRZ-OOK optical interconnects in a silicon photonics platform," *J. Lightw. Technol.*, vol. 35, no. 4, pp. 631–638, Feb. 15, 2017, doi: [10.1109/JLT.2016.2604839](https://doi.org/10.1109/JLT.2016.2604839).



**Alain Yuji Takabayashi** (Graduate Student Member, IEEE) received the M.Sc. degree in electrical engineering and information technology from Eidgenössische Technische Hochschule Zürich (ETHZ), in 2017. He is currently pursuing the Ph.D. degree with the Institute of Microengineering, École Polytechnique Fédérale de Lausanne (EPFL), Switzerland. His current research interests include the design, fabrication, and characterization of silicon photonic MEMS.



**Hamed Sattari** received the M.Sc. and Ph.D. degrees in photonics-telecommunication from the University of Tabriz, Iran, in 2010 and 2014, respectively. After his Ph.D., he joined the Research and Development Unit, Nanotechnology Research Center (NANOTAM), Bilkent University, Turkey, where he was designing plasmonic nano-antennas. In September 2016, he was awarded as a Swiss Government Excellence Scholarship holder for a postdoctoral position with the Q-Lab, École Polytechnique Fédérale de Lausanne (EPFL). Since September 2017, he has been involving in silicon photonics projects with goal of realizing MEMS-based reconfigurable components including switches, phase shifters, and variable optical attenuators.



**Pierre Edinger** received the joint M.Sc. degree in micro- and nanotechnologies for integrated systems from INPG Phelma, France, also from the Politecnico di Torino, Italy, and also from EPFL, Switzerland, in 2017. He is currently pursuing the Ph.D. degree with the Department of Micro and Nanosystems, KTH Royal Institute of Technology, Stockholm, Sweden. His current research interests include silicon photonics and MEMS.



**Peter Verheyen** received the degree in electrical engineering and the Ph.D. degree from Katholieke Universiteit Leuven, Leuven, Belgium, in 1996 and 2003, respectively. He was a Doctoral Researcher with the Interuniversity Microelectronics Center, Leuven, where he was involved in advanced CMOS integration and MEMS integration. He is with the Interuniversity Microelectronics Centre (imec) and is currently a member of the Silicon Photonics Staff as a part of the 3D Integration Group.



2005, he received the Steinmaur Foundation Nanotechnology Graduate Study Scholarship.

**Kristinn B. Gylfason** (Member, IEEE) received the B.Sc. and M.Sc. degrees in electrical engineering from the University of Iceland in 2001 and 2003, respectively, and the Ph.D. degree in electrical engineering from KTH in 2010. In 2015, he also received the title of Docent in micro- and nanosystems from KTH. From 2003 to 2005, he was a Research Engineer with Lyfjathroun Biopharmaceuticals, Iceland. He is currently an Associate Professor, leading the team with a focus on photonic nanodevices for biomedical and communications applications. In



Since 2016, he has been a full-time Professor with Ghent University, looking into novel topologies for large-scale programmable photonic circuits, supported by a consolidator grant of the European Research Council (ERC). He is currently a Professor with the Photonics Research Group, Ghent University, imec. His current research interests include the challenges for large-scale silicon photonics: Design methodologies and controllability of complex photonic circuits. He has a strong interest in telecommunications, information technology, and applied sciences. He is a Senior Member of the Optical Society of America (OSA) and SPIE.

**Wim Bogaerts** (Fellow, IEEE) received the Ph.D. degree in modeling, design, and fabrication of silicon nanophotonic components from Ghent University in 2004. During this work, he started the first silicon photonics process on imec's 200mm pilot line, which formed the basis of the multi-project-wafer service ePIXfab. In 2014, he co-founded Luceda Photonics, a spin-off company of Ghent University, imec, and also with the University of Brussels (VUB). Luceda Photonics develops unique software solutions for silicon photonics design, using the IPKISS design



**Niels Quack** (Senior Member, IEEE) received the M.Sc. degree from the École Polytechnique Fédérale de Lausanne (EPFL), Lausanne, Switzerland, in 2005, and the Dr.Sc. degree from Eidgenössische Technische Hochschule Zürich (ETH), Switzerland, in 2010. From 2011 to 2015, he was a Post-Doctoral Researcher and a Visiting Scholar with the University of California at Berkeley, Berkeley, CA, USA, within the Integrated Photonics Laboratory, Berkeley Sensor and Actuator Center. From 2014 to 2015, he was a Senior MEMS Engineer with Sercalo Microtechnology, Neuchâtel, Switzerland. He is currently a SNSF Assistant Professor with the École Polytechnique Fédérale de Lausanne (EPFL). He has authored or coauthored more than 50 articles in leading technical journals and conferences. His research interests include photonic micro- and nanosystems, with an emphasis on diamond photonics and silicon photonic MEMS. He is a Steering Committee Member of the IEEE International Conference on Optical MEMS and Nanophotonics (OMN) and a member of OSA and SPIE. He is a General Chair of the IEEE OMN 2018.

framework. Since 2016, he has been a full-time Professor with Ghent University, looking into novel topologies for large-scale programmable photonic circuits, supported by a consolidator grant of the European Research Council (ERC). He is currently a Professor with the Photonics Research Group, Ghent University, imec. His current research interests include the challenges for large-scale silicon photonics: Design methodologies and controllability of complex photonic circuits. He has a strong interest in telecommunications, information technology, and applied sciences. He is a Senior Member of the Optical Society of America (OSA) and SPIE.